Chemical Science

ROYAL SOCIETY OF CHEMISTRY

EDGE ARTICLE

View Article Online
View Journal

Cite this: DOI: 10.1039/d5sc06873h

All publication charges for this article have been paid for by the Royal Society of Chemistry

Impacting the balance between CO_2 and proton reduction by control over aggregation in a model π-conjugated N-heterocycle – proflavine†

Yana Reva, ‡[a] Jonas Färber, ‡[a] Yifan Bo, [a] Maximilian A. Thiele, [a] Christian Hanke,[b] Ayşe Günay-Gürer, [a] Maximillian Herm, [a] Johannes A. C. Barth[b] and Dirk M. Guldi *[a]

In this study, we investigated the mechanistic factors that govern the selective photocatalytic reduction of CO_2 over protons within a simple π-conjugated N-heterocycle, proflavine. Diluted conditions, where aggregates of 65 nm are formed, favored the selective CO_2 photo-reduction, while the gradual transition to concentrated conditions enabled photo-reductive H_2 generation. Proton reduction is coupled to larger aggregates, in which an alternative photo-relaxation pathway is active. We used transient absorption spectroscopy to corroborate that at low proflavine concentrations the presence of an electron donor triggers the one-electron reduced proflavine to perform the direct CO_2 reduction. At high proflavine concentrations, protonation of the one-electron reduced proflavine was favored due to a positive shift in basicity in larger aggregates with sizes over 1 μm. In turn, H_2 abstraction began with a pair of one-electron reduced, protonated, intermediates. Our study demonstrates an effective approach to limiting water reduction, a key challenge in advanced metal-free organic photocatalysis.

Received 5th September 2025
Accepted 8th May 2026

DOI: 10.1039/d5sc06873h

rsc.li/chemical-science

Introduction

Solar light-driven photocatalytic reduction of carbon dioxide (CO_2) in water has been demonstrated to be a promising pathway for sustainable energy conversion with the potential to reduce greenhouse gas emissions.[1] Despite significant progress in the field over the years, groundbreaking research continues to face emerging challenges. Competing water reduction, high prices for gas separation of valuable carbon-material from dihydrogen, and CO_2 recycling efficiency must be addressed.[2] For instance, to circumvent post-catalytic gas separation, the development of highly selective photocatalysts for CO_2 reduction is essential.

In photo-redox reactions, photocatalysts are excited, subsequently reduced by a suitable electron donor to finally produce a catalytically active species, that reduces the substrate by direct electron transfer.[3,4] The primary activation is crucial and involves bending of CO_2 and overcoming the negative reduction potential of −1.9 V *vs.* NHE.[5] Chemisorptive activation appears essential to lower the activation barrier and facilitate CO_2 reduction.[6] By tuning the electron-donating strength, light-activated reduction of the photocatalyst governs both its interactions with CO_2 and the subsequent substrate reduction. In contrast, protonation of the reduced photocatalyst deactivates the CO_2 reduction pathway, lowers its electronegativity, and creates favorable conditions for proton reduction and, therefore, H_2 generation.[7]

With a focus on the competing CO_2 and H^+ reduction, any change in the photocatalyst concentration commonly affects both pathways in the same way.[8–10] The scenario changes, however, as soon as aggregation comes into play. In metal-based photocatalysts, aggregation enhances the catalytic CO_2 reduction efficiency, while minimizing the competing water reduction.[11,12] A similar balance in organic, metal-free catalysts has not yet been extensively investigated, highlighting a significant knowledge gap. The intrinsic proton affinity of organic materials and pK_a shifts in aggregated systems[13–15] collectively suggest that aggregation is crucial for determining the photocatalytic selectivity. One prominent example of an efficient metal-free CO_2 reducing photocatalyst is covalent organic frameworks (COFs). COF's selective photo-reduction of CO_2 in aqueous solutions using visible light is remarkable.[16–18] COFs, which are constructed from π-conjugated N-heterocycles, are of particular interest here. For instance, Fu *et al.* found, that metal-free triazine-based COFs drive a clear-cut photocatalytic conversion of CO_2 to methanol, producing only trace amounts of H_2.[19] Hereby, π-conjugated N-atoms, which serve as photocatalytic centers in the triazine-building blocks,[20] play a crucial role.

[a]*Department of Chemistry and Pharmacy, Profile Center FAU Solar, Interdisciplinary Center for Molecular Materials (ICMM), Friedrich-Alexander-Universität Erlangen-Nürnberg, 91058 Erlangen, Germany. E-mail: dirk.guldi@fau.de*

[b]*Department Geographie und Geowissenschaften, Geozentrum Nordbayern, Friedrich-Alexander-Universität Erlangen-Nürnberg (FAU), Schlossgarten 5, 91054, Erlangen, Germany*

† Dedicated to Jonathan Sessler on the occasion of his 70th birthday.

‡ These authors contributed equally.

In this work, we address the nuanced interplay between aggregation and selectivity in the reduction of CO_2 over protons. The model system proflavine – a π-conjugated N-heterocycle was utilized. Considering both, the ability to form aggregates[21] and a suitable pH window to tune the de-/protonation of the active photoreduced species,[22,23] proflavine represents an excellent model.

In the ground state at pH 7, proflavine exists primarily in its single protonated form, as **(Pf-H)**$^+$ (Fig. 1a).[24–28] Following photoexcitation at 443 nm and intersystem crossing (ISC) under deoxygenated conditions, the long-lived triplet excited state (T_1)**(Pf-H)**$^+$ emerges.[27,29] In the presence of an electron donor, such as TEOA, (T_1)**(Pf-H)**$^+$ with an energy of 2.17 eV accepts an electron and is transformed into the reduced **(Pf-H)**$^\bullet$ (Fig. 1a). Because of its reduction potential of −1.57 V *vs.* SHE **(Pf-H)**$^\bullet$ is active in numerous photo-redox reactions.[22,24,30–33] The reduced species exhibits a pK_a value of 4.5 and, therefore, forms **(Pf-H$_2$)**$^{\bullet+}$ under acidic conditions (Fig. 1a).[23] Noticeably, electron-rich and conjugated nitrogen atoms are present. Thus, we hypothesise that **(Pf-H)**$^\bullet$ chemisorbs CO_2 at the electron-deficient carbon site and then facilitates its reduction. Additionally, aggregate formation is thought to be beneficial for altering its proton affinity, a key step for protonation and thus for H_2 generation.

Results and discussion

Photocatalysis

N-conjugated organic metal-free photocatalysts commonly generate single-carbon compounds like CO, HCOOH, HCHO, CH_3OH, and CH_4, with a maximum of 8 transferred electrons.[16–20] The photocatalytic CO_2 reduction was performed with 25 μM **(Pf-H)**$^+$ in aqueous solutions containing 4.28 vol% TEOA and 0.55 M KH_2PO_4 at a pH of 7. The reaction mixture was first saturated with high purity CO_2, minimizing O_2 contamination, and then irradiated with a Xe-lamp using a 1.5 AM filter (1 sun). Under these conditions, gas-phase analysis after 1 h of irradiation afforded 0.1 nmol CO, 0.3 nmol CH_4, and no H_2 (Fig. 1b).§ When omitting either the electron donating TEOA or the buffering KH_2PO_4 or keeping non-irradiated samples, only traces of CH_4 and CO were discernible. These results demonstrate the successful photocatalytic reduction of CO_2 mediated by proflavine.¶ To optimize the catalytic conditions, the pH was varied between 6 and 8.5 by altering the KH_2PO_4 concentration. Hereby, a pH of 7 was found to deliver the maximum amount of CH_4 and CO (Fig. S1). Next, we changed the **(Pf-H)**$^+$ concentrations and examined the photocatalysis during an illumination period of one hour (Fig. 1c). The selected concentration range was given by the absence of discernible products. At a **(Pf-H)**$^+$ concentration of 25 μM, the highest amounts of CH_4 and CO were monitored. Notably, no other products such as HCOOH, HCHO, or CH_3OH were detected under such optimized conditions (Fig. S2). Of great interest is the fact that at **(Pf-H)**$^+$ concentrations larger than 200 μM, the generation of H_2 dominated that of CH_4 and CO. For example, at 410 μM, only traces of CH_4 are detectable, while H_2 levels reached a maximum of 3.25 nmol h^{-1}. At 1000 μM, photocatalysis only yields H_2 without any significant amount of CH_4 or CO. The lack of any CO_2 formation at high **(Pf-H)**$^+$ concentrations proves that

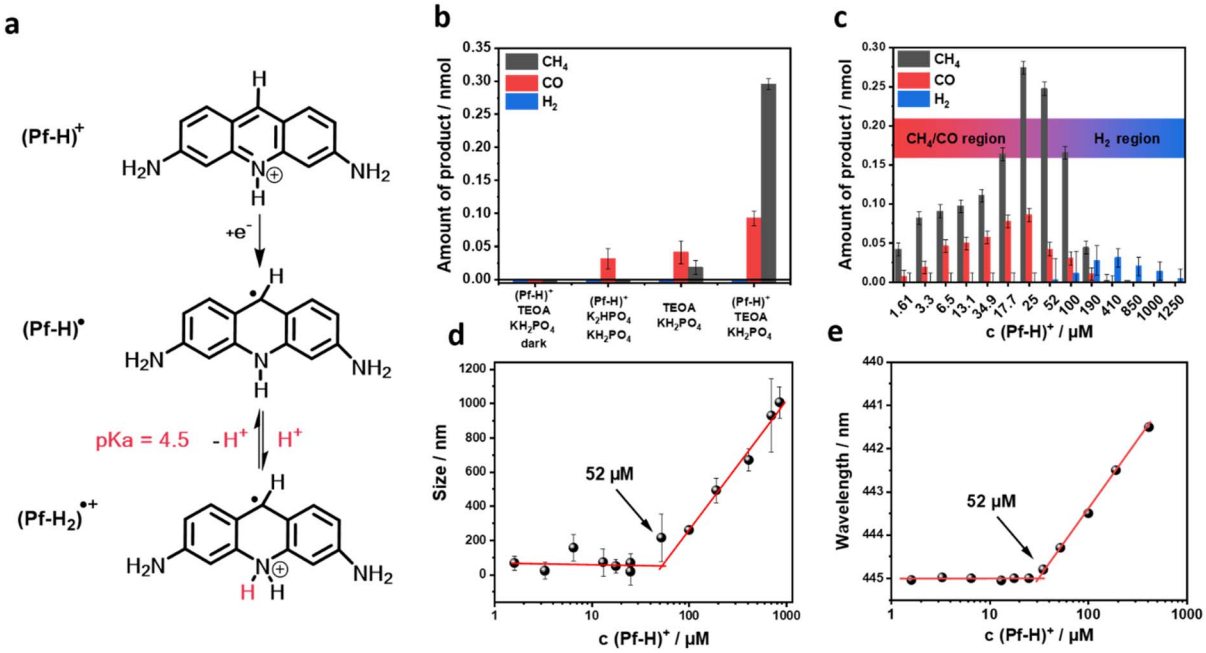

Fig. 1 (a) Relevant structures. (b) Rate of CH_4, CO, and H_2 evolution for references at pH 7 after 1 h upon 1 sun irradiation with a Xe-lamp equipped with 1.5 AM filter. (c) Rate of CH_4, CO, and H_2 evolution measured in aqueous solution of 4.28 vol% TEOA, 0.55 M KH_2PO_4, at pH 7, and with different concentrations of **(Pf-H)**$^+$ over 1 hour of irradiation. (d) DLS analysis in aqueous solution of 4.28 vol% TEOA, 0.55 M KH_2PO_4, at pH 7, and with different concentrations of **(Pf-H)**$^+$. (e) Concentration-dependent shift in absorbance of aqueous solutions with 4.28 vol% TEOA, 0.55 M KH_2PO_4, and at pH 7.

none of the photo-products, that is, CH_4 or CO, stem from the photo-decomposition of the catalyst. Additionally, we compared two identical photocatalytic systems, both containing 25 μM **(Pf-H)$^+$**, at the optimized photocatalytic conditions. One system was purged with CO_2 and the other with O_2 (supporting superoxide-mediated decomposition) prior to irradiation. The O_2-purged sample failed to generate any detectable CH_4 after one hour of irradiation. Conclusively, the observed CH_4 is produced exclusively in the photocatalytic reduction of CO_2 by proflavine (Fig. S3). The competition between CO_2 and H^+ reduction must be influenced by the intrinsic properties of the catalyst. This conclusion is further supported by the selective CO_2 reduction occurring even in solutions at high proton concentrations.

Considering the aforementioned results, we not only infer two different photo-relaxation pathways, but also their dependence on the photocatalyst concentration. To elaborate on the nature of the concentration-dependent CO_2/H^+ reduction selectivity, dynamic light scattering (DLS) was measured under optimized photocatalytic conditions, with a **(Pf-H)$^+$** concentration ranging from 1.6 to 850 μM (Fig. 1d). At concentrations below 52 μM, **(Pf-H)$^+$** forms aggregates with an average size of 65 nm in the presence of 4.28 vol% TEOA and 0.55 M KH_2PO_4 (pH 7). At 52 μM dihydrogen is generated and the aggregate size notably increases. At 1000 μM, where photocatalysis yields solely H_2, the average size of the aggregates reached 1 μm. The absorption spectra of **(Pf-H)$^+$** across different concentrations were examined (Fig. S4). Starting at around 52 μM, a stepwise blue-shift in the absorption maximum from 445 to 441 nm along with the emergence of a shoulder at 482 nm were observed. This supports the notion that aggregates are growing when a critical concentration of **(Pf-H)$^+$** is passed (Fig. 1e). To this end, photocatalytic tests using 1000 μM **(Pf-H)$^+$** in aqueous solutions containing 4.28 vol% TEOA were conducted and the pH was changed from 6.5 to 10 by varying KH_2PO_4 (Fig. S5). Importantly, below a pH of 7 all photo-products relate to the H^+ reduction. Going beyond a pH of 7, CO_2 reduction products were found next to those stemming from H^+ reduction.‖ Aggregation has caused a shift in the pK_a of the active species, **(Pf-H)$^\bullet$**. A stronger basicity facilitates the protonation, on one hand, and enhances H_2 generation, on the other hand.

CO_2 reduction mechanism

The reduced form of proflavine, **(Pf-H)$^\bullet$**, was prepared by chemically reducing **(Pf-H)$^+$** with $LiAlH_4$. The product solution was then filtered and the pH adjusted to 7 by adding hydrochloric acid. An important fingerprint of **(Pf-H)$^\bullet$** is its 394 nm absorption (Fig. S6).

Further, mass spectrometry with the chemically generated **(Pf-H)$^\bullet$** was conducted and a mass of 209.01 m/z was found in the negative ion mode. This is in good agreement with the corresponding isotope pattern (Fig. S7).** Additionally, a titration of **(Pf-H)$^\bullet$** under inert atmosphere corroborates the 446 nm fingerprint of protonation below a pH of 4.5. Corresponding titration curves and spectra are all gathered in Fig. S9. In another experiment, we saturated a **(Pf-H)$^\bullet$** solution with CO_2 and noted a red-shift of the absorption to 443 nm. Implicit is the re-oxidation of **(Pf-H)$^\bullet$** and regeneration of **(Pf-H)$^+$** (Fig. S10). Moreover, the gaseous products generated upon CO_2 saturation of **(Pf-H)$^\bullet$**, namely CO and CH_4, were analysed. This data was compared with that recorded for a CO_2-saturated solution of **(Pf-H)$^+$** at 25 μM, which lacked any CO_2 reduction (Fig. S11). **(Pf-H)$^\bullet$** showed a striking kinetic selectivity: while it exhibited high stability against re-oxidation by O_2 (only 2% re-oxidized after 24 hours in 99.9% O_2), it underwent full and instant re-oxidation when exposed to CO_2, confirming the CO_2 pathway's kinetic preference (Fig. S12). Given the absence of an electron donor, buffer or photoirradiation, CO and CH_4 unambiguously stem from the direct CO_2 reduction. Hence, we postulate that **(Pf-H)$^\bullet$** is a key species in the photocatalytic CO_2 reduction.

To provide unambiguous evidence for the carbon conversion pathway, we monitored the $^{13}C/^{12}C$ ratios in both CO_2 and CH_4 using wavelength-scanned cavity ring-down spectroscopy. The $^{13}C/^{12}C$ ratios are expressed in a delta notation as a permille deviation from Vienna Pee Dee Belemnite (*i.e.* $\delta^{13}C$ in ‰ VPDB) as standard. They were determined for CO_2 and CH_4 in the complete photocatalytic system and solutions in the absence of an electron donor, buffer or photoirradiation (Table S1).†† The originally added CO_2 had a $\delta^{13}C$ value of −41.6‰. It was only upon CO_2 addition together with all other additives that we found significant CH_4 yields. Under these conditions, $\delta^{13}C_{CO_2}$ decreased by a maximum of 7.0‰. At the same time, any detectable CH_4 was around an average of −37.3‰. From these findings we conclude that CH_4 stems from CO_2 reduction with a preferential uptake of ^{13}C. Additionally, the $^{13}C/^{12}C$ ratios for any dissolved organic carbon (doc) were measured by isotope ratio mass spectrometry with and without irradiation (Table S2). Our $\delta^{13}C_{doc}$ measurements lacked any deviations, but differed noticeably from the $\delta^{13}C$ of generated CH_4. Negligible differences in $\delta^{13}C_{doc}$ – with and without irradiation – coupled with their significant deviations from $\delta^{13}C_{CH_4}$ confirms that CH_4 is not a by-product of any organic material decomposition.

To gather additional information on the photoreduction mechanism proflavine was deposited onto a platinum surface and electrochemical *operando* Raman spectroscopy was conducted. The aqueous phase was purged with CO_2 and KH_2PO_4/K_2HPO_4 were added to adjust the pH to 7. Broad fingerprints between 750 and 1750 cm^{-1} were taken as evidence for the proflavine stability at 0 V *vs.* Ag/AgCl. Under reductive conditions, that is, −1.5 V *vs.* Ag/AgCl, new features emerged as evident from the corresponding differential spectrum. Compared to reference measurements at 0 V *vs.* Ag/AgCl, the spectral changes at −1.5 V *vs.* Ag/AgCl revealed broad signals with distinguishable peaks around 1307 and 2208 cm^{-1}, corresponding to symmetric –C–O stretching vibration of a carboxylate-like species (CO_2 adsorption) and –C≡O stretching vibration (CO adsorption), respectively (Fig. S13). These features are the crucial intermediates in the formation of CO and CH_4. Their presence confirms the successful adsorption and subsequent reduction of CO_2 by proflavine.

Photodegradation

Proflavine is known to undergo side reactions during photocatalysis.[27] To demonstrate, that such side reactions have

minimal impact on the product selectivity, 25 μM **(Pf-H)**$^+$ were photoirradiated in the presence of 4.28 vol% TEOA and 0.55 M KH_2PO_4 for four hours rather than one (Fig. S14).‡‡ In parallel, the absorption spectrum of the liquid phase was monitored (Fig. S15). CO and CH_4 increase during the photoirradiation. Importantly, no appreciable H_2 was detected. It is, however, noted that after three hours, the generation rates of the products plateaued and decayed, likely due to the disproportionation of **(Pf-H)**$^+$. A continuous decrease of the 445 nm absorption and the concurrent formation of dihydroproflavine and leuco-proflavine with their characteristic absorptions at 295 and 340 nm, respectively, validates the disproportionation.[27] Based on these findings, we demonstrated that the product selectivity is not impacted by the formation of any side products.

Excited state spectroscopy at low concentrations – 65 nm aggregates

First, fs-TA for an aqueous buffered solution (with 0.5 M K_2HPO_4/KH_2PO_4) of 25 μM **(Pf-H)**$^+$ without any electron donor was considered. fs-TA spectra were deconvoluted with a kinetic model based on two species and two evolution-associated spectra (EAS), that is, EAS-1 and EAS-2 (Fig. S16), were obtained.

EAS-1, for which a lifetime of 3.8 ps was determined, showed excited state absorptions (ESAs) at 400 nm, ground state bleaching (GSB) at 445 nm, and stimulated emission (SE) at 515 nm. All of them are in excellent agreement with the steady state absorption and fluorescence spectra of (S_0)**(Pf-H)**$^+$ (Fig. S17). As the decay of EAS-2 is outside the fs-TA timescale, we conducted additional ns-TA experiments. ns-TA spectra were also fitted obtaining two EASs, that is, EAS-2 and EAS-3 (Fig. S18). The characteristics of EAS-2, which include ESA at 400 nm, GSB at 445 nm, and SE at 515 nm, are like those of EAS-1. From the similarity between EAS-1 and EAS-2 it was concluded, that the two are a vibrationally hot singlet excited state (S_1^{hot})**(Pf-H)**$^+$ and a vibrationally relaxed singlet excited state (S_1^{rel})**(Pf-H)**$^+$, respectively. After 4.7 ns, SE is replaced by ESAs < 390 nm and between 500 and 750 nm. These comprise EAS-3 and feature a lifetime of 29.2 μs. In line with sensitization experiments using $(Ir[dF(CF_3)ppy]_2(dtbpy))PF_6$ as a triplet sensitizer,[34] EAS-3 is attributed to the triplet excited state – (T_1)**(Pf-H)**$^+$.§§ All reference experiments are summarized in Fig. S19–S21.

In the next set of our experiments TEOA was added: 25 μM **(Pf-H)**$^+$, 0.55 M KH_2PO_4, and 4.28 vol% TEOA. On the fs-TA timescale, the only fully resolvable EAS was that of EAS-1 with 450 nm GSB and 515 nm SE. It is the (S_1^{hot})**(Pf-H)**$^+$ (Fig. S22). Its lifetime is with 7.5 ps slightly longer than the reference experiments. On the ns-TA timescale, the data was taken and best deconvoluted when using a three species kinetic model (Fig. 2). EAS-2 is also like in the experiments without TEOA – albeit being lower in intensity – identified as (S_1^{rel})**(Pf-H)**$^+$. It takes 4.5 ns, by which EAS-2 gives place to EAS-3, namely a localized (T_1)**(Pf-H)**$^+$. Notably, (T_1)**(Pf-H)**$^+$ is in the presence of TEOA shorter-lived than in the absence of TEOA; 4.5 *versus* 29.2 μs.

To gather insights into the TEOA-induced quenching of **(Pf-H)**$^+$, we conducted ns-TA at different TEOA concentrations. The pH was kept constant at 7 by means of adjusting the KH_2PO_4 concentrations. Results were quantitatively treated with the Stern–Volmer relationship, $\tau_0/\tau = 1 + K_{SV}[TEOA]$, in which K_{SV} is the Stern–Volmer constant, [TEOA] is the concentration of TEOA, and τ_0 and τ are the (T_1)**(Pf-H)**$^+$ lifetimes in the absence and presence of TEOA, respectively. The linear relationship was ascribed to the dynamic electron-transfer quenching of (T_1)**(Pf-H)**$^+$ by TEOA.¶¶ With the K_{SV} of 16.4 M^{-1} the bimolecular quenching rate constant (K_q) was calculated to be 5.6×10^5 M^{-1} s^{-1} (Fig. S23). A low K_q is attributed to the partial protonation of TEOA at pH 7 due to a pK_a value of 7.76, lowering the concentration of its unprotonated, electron-donating form. Therefore, the presence of protonated TEOA limits the rate constant well below the diffusion-controlled limit.

The quenching of (T_1)**(Pf-H)**$^+$ by the electron donating TEOA resulted in EAS-4, for which a distinct 388 nm ESA and a lifetime outside the time-range of our ns-TA set-up were derived. Considering a significant spectral overlap of the differential **(Pf-H)**$^\bullet$ − **(Pf-H)**$^+$ and EAS-4 as well as the presence of an electron-donating TEOA, EAS-4 is assigned to **(Pf-H)**$^\bullet$ (Fig. S24). Fig. 2e summarizes the proposed mechanism for the low concentration experiments – aggregate size 65 nm.

To exclude any impact of TEOA degradation products onto the proposed mechanism, ns-TA was conducted with 25 μM **(Pf-H)**$^+$ in water, using 4.28 vol% methanol rather than TEOA as electron donor. The raw data was deconvoluted with a kinetic model based on three species (Fig. S25). All three EASs match those discussed when employing electron donating TEOA and, in turn, prove its electron donation.

Excited state spectroscopy at intermediate concentrations – 700 nm aggregates

A systematic increase in **(Pf-H)**$^+$ concentration alters the product distribution from an exclusive CO/CH_4 mixture to one also featuring H_2 (Fig. 1c). Mechanistic aspects were investigated by using aqueous solutions of pH 7 with 410 μM **(Pf-H)**$^+$, 0.55 M KH_2PO_4, and K_2HPO_4.

Global analyses of fs-TA reveal two consecutively emerging EAS, that is, EAS-1 and EAS-2. They correspond to (S_1^{hot})**(Pf-H)**$^+$ and (S_1^{rel})**(Pf-H)**$^+$ and match the spectral characteristics seen in the low concentration regime (Fig. S26). It takes 3.2 ps for (S_1^{hot})**(Pf-H)**$^+$ to interconvert into (S_1^{rel})**(Pf-H)**$^+$. To determine the lifetime of EAS-2 we conducted ns-TA. Interpretation of the 410 μM **(Pf-H)**$^+$ ns-TA experiments required a kinetic model based on three species, that is, EAS-2, EAS-3, and EAS-4 (Fig. S27). EAS-2 are similar on the fs- and ns-time scales. The lifetime of (S_1^{rel})**(Pf-H)**$^+$) is 5 ns. EAS-3 and EAS-4 exhibit similar spectral properties: ESAs < 390 nm and between 500 and 750 nm. To this end, EAS-3 and EAS-4 both are attributed to (T_1)**(Pf-H)**$^+$s; one short-lived with a lifetime of 1 μs, and one long-lived with a lifetime of 33 μs. We hypothesize that the 1 μs component of (T_1)**(Pf-H)**$^+$ is due to triplet–triplet annihilation and that it is activated by the high **(Pf-H)**$^+$ concentration.

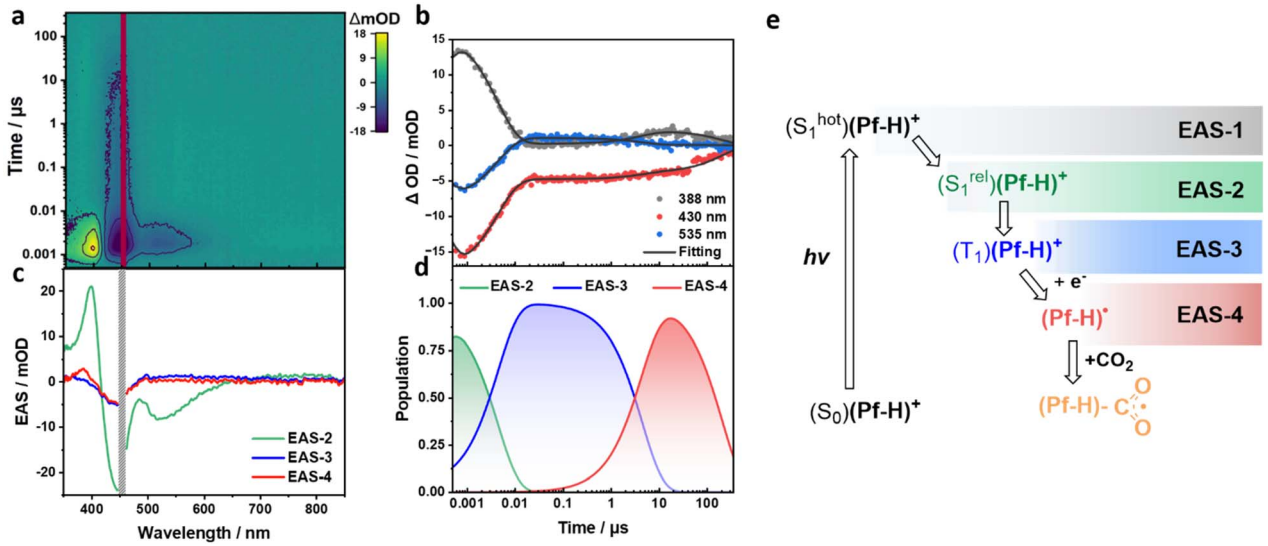

Fig. 2 (a) ns-TA heat map of 25 μM $(Pf\text{-}H)^+$ in aqueous solutions with 4.28 vol% TEOA and 0.55 M KH_2PO_4. The photoexcitation wavelength was set to 450 nm. (b) Representative time traces at 388, 430, and 535 nm depicting the recorded evolution of the transients. (c) Evolution associated spectra (EAS) from the sequential three-exponential global analyses of the ns-TA spectra. EAS-2, EAS-3, and EAS-4 correspond to $(S_1^{rel})(Pf\text{-}H)^+$ with a lifetime of 4.5 ns, $(T_1)(Pf\text{-}H)^+$ with a lifetime of 4.5 μs, and $(Pf\text{-}H)^\bullet$, respectively. (d) Time profiles depicting the time-resolved population of the corresponding EASs from global analyses of the ns-TA spectra. (e) Corresponding mechanistic cascade of transient states.

fs-TA spectroscopy of the TEOA-containing aqueous system with 410 μM $(Pf\text{-}H)^+$, 4.28 vol% TEOA, and 0.55 M KH_2PO_4 gives rise to two EASs. For EAS-1, 400 nm ESA and 440 nm GSB are complemented by 515 nm SE (Fig. S28). This $(S_1^{hot})(Pf\text{-}H)^+$ lives for 33.3 ps and undergoes relaxation to afford $(S_1^{rel})(Pf\text{-}H)^+$. Insights into the decay of $(S_1^{rel})(Pf\text{-}H)^+$ came from ns-TA measurements. Fitting the ns-TA spectrum requires the use of four species rather than three like in the absence of TEOA.

For EAS-2, once again, 400 nm ESA, 440 nm GSB, and 515 nm SE due to (S_1^{rel}) are noted. (S_1^{rel}) undergoes intersystem crossing within 4.5 ns to afford $(T_1)(Pf\text{-}H)^+$ in the form of EAS-3 based on ESAs < 390 nm and between 500 and 750 nm (Fig. 3). Rather than undergoing ground state recovery as in the case of TEOA-free conditions, $(T_1)(Pf\text{-}H)^+$ decays quickly in the presence of 4.28 vol% TEOA within 2.1 μs. A 35.5 μs lived EAS-4 evolves from the interaction of $(T_1)(Pf\text{-}H)^+$ with the electron donating TEOA. The most prominent ESAs are discernible at 388 and 450 nm. As shown previously, $(Pf\text{-}H)^\bullet$ protonation causes a rise of a 446 nm feature, which is assigned to $(Pf\text{-}H_2)^{\bullet+}$. To deconvolute the spectral signature of EAS-4, EAS-3 was subtracted from EAS-4. The resulting differential spectrum combines the spectral features of $(Pf\text{-}H)^\bullet$ next to those of $(Pf\text{-}H_2)^{\bullet+}$ (Fig. S30). The final species, namely EAS-5, is an amplification of the 446 nm ESA and, therefore corresponds to a second $(Pf\text{-}H_2)^{\bullet+}$. Its lifetime is outside of the time-range covered by our ns-TA set-up. In stark contrast to the experiments at low $(Pf\text{-}H)^+$ concentrations, protonation of $(Pf\text{-}H)^\bullet$ and formation of $(Pf\text{-}H_2)^{\bullet+}$ are observable on the microsecond timescale, due to an increase in proton affinity of the reduced proflavine in the aggregates. Evidently, at the given concentrations a competing photocatalytic path evolves. A somewhat broader size distribution of aggregate sizes at the concentration of 410 μM renders the deconvolution of $(Pf\text{-}H)^\bullet$ and $(Pf\text{-}H_2)^{\bullet+}$ and detection thereof impossible.*** Fig. 3e summarizes the proposed mechanism for intermediate concentrations of proflavine (700 nm-aggregate).

Excited state spectroscopy at high concentrations – 1 μm-aggregates

Given the overlapping absorbance of $(Pf\text{-}H)^+$ and $(Pf\text{-}H_2)^{\bullet+}$, a clear differentiation between GSB and the evolution of $(Pf\text{-}H_2)^{\bullet+}$ mandates additional investigations. To this end, we considered a $(Pf\text{-}H)^+$ concentration that would shift the photo-activity to the exclusive H_2 formation. As such, fs-TA of aqueous solution with 1000 μM $(Pf\text{-}H)^+$, 4.28 vol% TEOA, and 0.55 M KH_2PO_4 was recorded. Global fitting revealed two EASs upon sequential deconvolution. EAS-1 with a SE at 515 nm is assigned to $(S_1^{hot})(Pf\text{-}H)^+$ and lives for 63 ps (Fig. S32). EAS-2 outlives the ps-timescale. Therefore, we proceeded with ns-TA and used a global fit with a kinetic model based on four species (Fig. 4). After 3.6 ns, EAS-2 with the spectral fingerprints of $(S_1^{rel})(Pf\text{-}H)^+$ is replaced by EAS-3 with an intrinsic lifetime of 3 μs. EAS-3 is characterized by ESAs between 500 and 750 nm, which are the known $(T_1)(Pf\text{-}H)^+$ characteristics.

Following its 3 μs lasting decay, ESAs > 500 nm of EAS-4 are formed as $(Pf\text{-}H_2)^{\bullet+}$ grows. For the latter, a lifetime of 43.6 μs was derived. Notably, it was impossible to deconvolute $(Pf\text{-}H)^\bullet$ found at the lower concentrations. We rationalize this fact by a pK_a-driven shift towards $(Pf\text{-}H_2)^{\bullet+}$ rather than $(Pf\text{-}H)^\bullet$.

Subsequently, EAS-5 evolves and is linked to the intensification of the ESA > 500 nm. EAS-5 lifetime extends beyond the temporal window of our ns-TA set-up. While the high $(Pf\text{-}H)^+$ concentration of 1000 μM leads to strong ground-state absorbance that obscures the near-UV region, the emergence of the

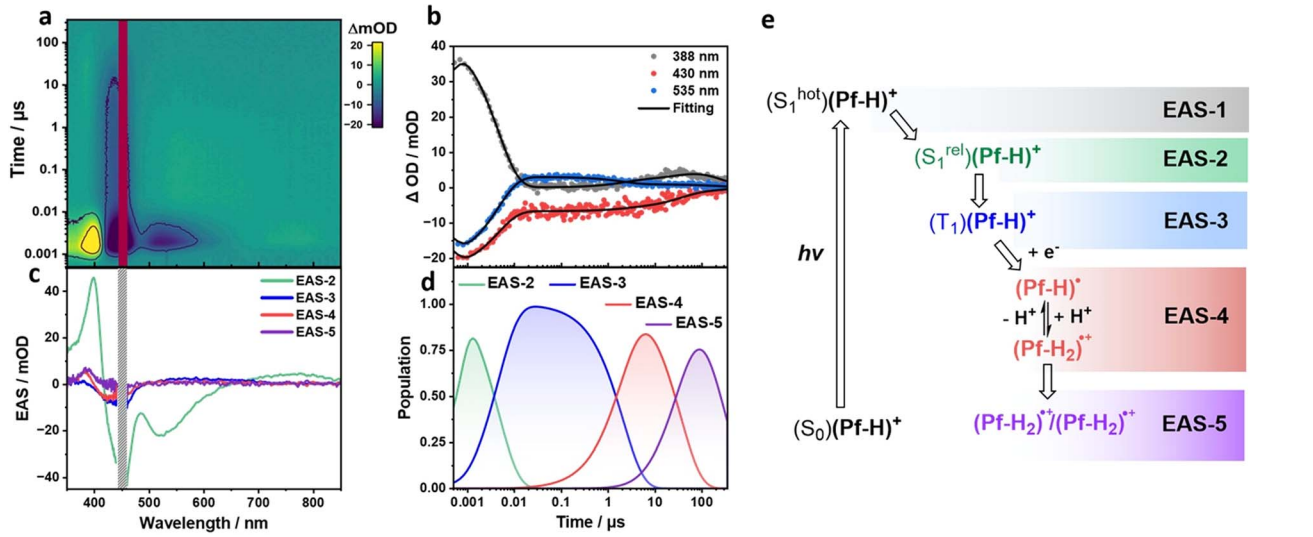

Fig. 3 (a) ns-TA heat map of 410 μM $(Pf\text{-}H)^+$ in aqueous solutions with 4.28 vol% TEOA and 0.55 M KH_2PO_4. The photoexcitation wavelength was set to 450 nm. (b) Representative time traces at 388, 430, and 535 nm depicting the recorded evolution of the transients. (c) Evolution associated spectra (EAS) from the sequential four-exponential global analyses of the ns-TA spectra. EAS-2, EAS-3, EAS-4, and EAS-5 correspond to $(S_1^{rel})(Pf\text{-}H)^+$ with a lifetime of 4.5 ns, $(T_1)(Pf\text{-}H)^+$ with a lifetime of 2.1 μs, $[(Pf\text{-}H)^\bullet \leftrightarrow (Pf\text{-}H_2)^{\bullet+}]$ with a lifetime of 35.5 μs, and $(Pf\text{-}H_2)^{\bullet+}/(Pf\text{-}H_2)^{\bullet+}$, respectively. (d) Time profiles depicting the time-resolved population of the corresponding EASs from global analyses of the ns-TA spectra. (e) Corresponding mechanistic cascade of transient states.

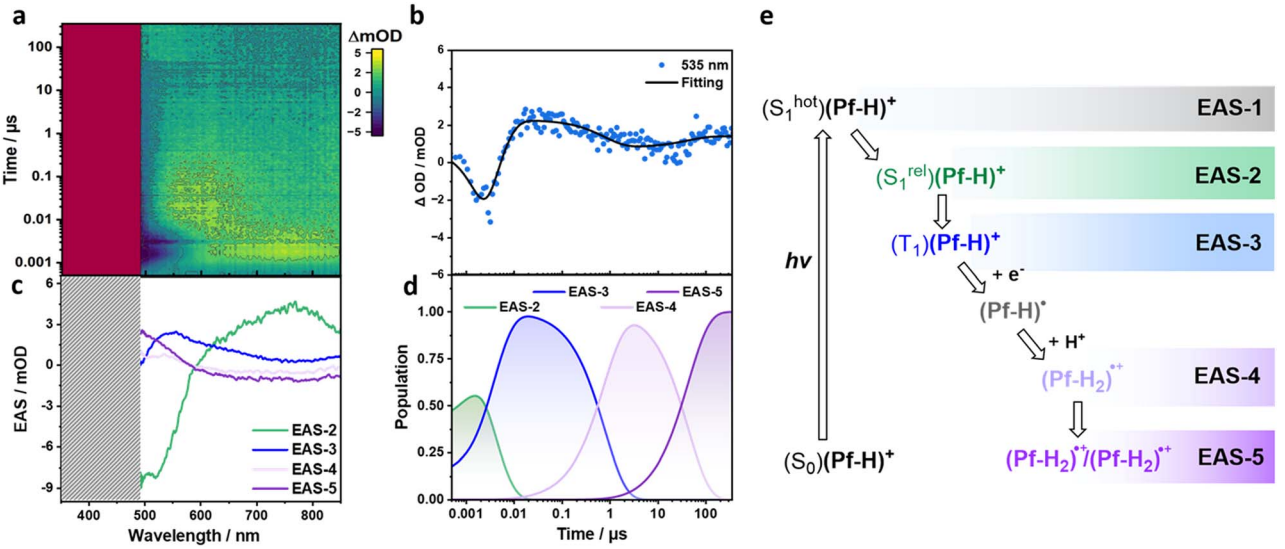

Fig. 4 (a) ns-TA heat map of 1000 μM $(Pf\text{-}H)^+$ in aqueous solutions with 4.28 vol% TEOA and 0.55 M KH_2PO_4. The photoexcitation wavelength was set to 450 nm. (b) Representative time trace at 535 nm depicting the recorded evolution of the transients. (c) Evolution associated spectra (EAS) from the sequential four-exponential global analyses of the ns-TA spectra. EAS-2, EAS-3, EAS-4, and EAS-5 correspond to $(S_1^{rel})(Pf\text{-}H)^+$ with a lifetime of 3.6 ns, $(T_1)(Pf\text{-}H)^+$ with a lifetime of 3 μs, $(Pf\text{-}H_2)^{\bullet+}$ with a lifetime of 43.6 μs, and $(Pf\text{-}H_2)^{\bullet+}/(Pf\text{-}H_2)^{\bullet+}$, respectively. (d) Time profiles depicting the time-resolved population of the corresponding EASs from global analyses of the ns-TA spectra. (e) Corresponding mechanistic cascade of transient states.

$(Pf\text{-}H_2)^{\bullet+}$ ESA is still evident, and its gradual intensification is clearly supported. Consequently, after the initial $(Pf\text{-}H_2)^{\bullet+}$ is produced, a second $(Pf\text{-}H_2)^{\bullet+}$ forms.

Our previous investigations with N-heterocyclic phenazine aggregates demonstrated that TEOA facilitated the formation of the second reduced and protonated phenazine *via* a chemical reduction that is linked to TEOA's self-oxidation reaction.[7] In ns-TA, an intensification of the characteristic ESAs reflects the second reduction and protonation. Seeing a similar behavior in proflavine-aggregates, we conclude that the reduction of $(T_1)(Pf\text{-}H)^+$ and the formation of $(Pf\text{-}H)^\bullet$ is linked to a positive pK_a shift in the 1 μm-aggregates. This facilitates protonation to afford $(Pf\text{-}H_2)^{\bullet+}$. $(Pf\text{-}H_2)^{\bullet+}$ subsequently reacts with a second $(Pf\text{-}H_2)^{\bullet+}$ before H_2 is released. Fig. 4e summarizes the proposed

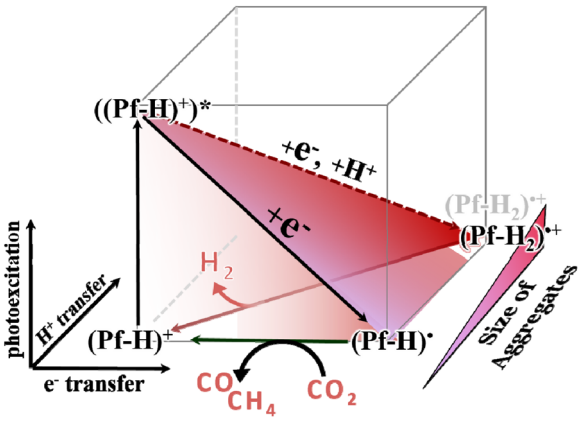

Fig. 5 Electronic ground- and excited state square scheme in proflavine at pH 7 in the presence of electron donating TEOA.

mechanism for high concentrations of proflavine – aggregate size of 1 μm.

Conclusions

We demonstrated that the degree of clustering functions as a molecular ruler that regulates the balance between photocatalytic CO_2 and proton reduction in organic π-conjugated N-heterocyclic compounds, a consideration not previously reported in the literature. In this context, under dilute conditions, that is, small aggregate clusters, **(Pf-H)**$^+$ photocatalysis predominantly yields CO_2 reduction products. Proven by means of fs-TA and ns-TA spectroscopy, the addition of an electron donor enables the photo-induced formation of **(Pf-H)**$^\bullet$, that is, the reduced form of **(Pf-H)**$^+$. **(Pf-H)**$^\bullet$ is, on one hand, stable in the absence of CO_2 and, on the other hand, the catalytically active species that performs CO_2 reduction. For example, exposing a solution of chemically reduced **(Pf-H)**$^\bullet$ to CO_2 resulted in its full re-oxidation together with CO and CH_4 generation.

Once the critical concentration is passed, the formation of H_2 starts to compete with the CO_2 reduction. This concentration represents a threshold beyond which the degree of clustering gradually increases. Based on fs-TA and ns-TA spectroscopy larger aggregates enforce the protonation of **(Pf-H)**$^\bullet$, yield **(Pf-H$_2$)**$^{\bullet+}$, and allow for H_2 release upon reaction with a second **(Pf-H$_2$)**$^{\bullet+}$. This reactivity is attributed to a positive shift in the pK_a of reduced proflavine at higher degrees of clustering. The intricate nature of this aggregation process provides a fertile ground for further investigation, opening up new avenues for understanding and controlling the mechanism of organic photocatalysts. Fig. 5 summarizes the complete mechanism.

Author contributions

Y. R.: conceptualization of the involved mechanism, writing – original draft. Y. R. and J. F.: formal analysis, investigation of the photocatalytic activity and the involved photorelaxation cascade, data validation and visualization. M. A. T. and A. G.-G. confirmed absence of liquid-phase CO_2 reduction products. J. F. Y. B. and M. H.: mechanism validation. M. A. T.: formal analysis of DLS. J. F. and C. H. isotope measurements. J. A. C. B. and D. M. G.: supervision, project administration and finding acquisition. All authors contributed to the final version – review & editing.

Conflicts of interest

There are no conflicts to declare.

Data availability

The data supporting this article have been included as part of the supplementary information (SI). Supplementary information: materials, experimental procedures, characterizations, SI Fig. S1–S25. See DOI: https://doi.org/10.1039/d5sc06873h.

Notes and references

§ The corresponding values were further used as references and subtracted to reveal the amount of photocatalytically generated products.

¶ The reported product yields are not normalized by turnover number (TON) due to the observed degradation of the photocatalyst over time. This instability implies that the catalyst's activity diminishes throughout the reaction period, making traditional TON calculations unrepresentative of the system's true catalytic efficiency.

‖ The concentration of H_2 has remained constant.

** Storing a **(Pf-H)**$^\bullet$ solution for 24 h confirmed its inertness in water (Fig. S8).

†† The increased concentration of CH_4 in the isotopic measurements are explained, as here a different setup was used, which demanded a decreased gas to liquid phase ratio in the containers paired with an increased irradiation surface of the vessels.

‡‡ The gaseous phase was analyzed and the sample was re-purged with CO_2 every 30 min.

§§ ns-TA in oxygen-free methanol solutions of $(Ir[dF(CF_3)ppy]_2(dtbpy))PF_6$ and **(Pf-H)**$^+$ resulted in a 1.38 μs lasting formation of ESAs < 390 and between 500 and 750 nm that decayed with 28.2 μs.

¶¶ In order to reach pH 7, the TEOA-free sample was buffered with KH_2PO_4 and K_2HPO_4. Different electrolyte-composition causes an offset of the τ_0 value, deviating the linear behavior and, therefore was excluded from fitting.

‖‖ The corresponding time-trace fits and singular value decompositions of the residual matrices corroborate the choice of four (Fig. S29).

**** The model fitting with five species does not sufficiently resolve **(Pf-H)**$^\bullet$ and **(Pf-H$_2$)**$^{\bullet+}$ separately (Fig. S31).

1 Ž. Kovačič, B. Likozar and M. Huš, Photocatalytic CO_2 Reduction: A Review of Ab Initio Mechanism, Kinetics, and Multiscale Modeling Simulations, *ACS Catal.*, 2020, **10**, 14984–15007.

2 X. Ma, J. Albertsma, D. Gabriels, R. Horst, S. Polat, C. Snoeks, F. Kapteijn, H. B. Eral, D. A. Vermaas, B. Mei, S. de Beer and M. A. van der Veen, Carbon monoxide separation: past, present and future, *Chem. Soc. Rev.*, 2023, **52**, 3741–3777.

3 F. Mohamadpour, Acridine yellow G as a photo-induced electron transfer catalyzed radical metal-free synthesis of tetrahydrobenzo[b]pyran scaffolds in an aqueous media, *Curr. Res. Green Sustainable Chem.*, 2023, **6**, 100356.

4 M. Yamawaki, A. Asano, T. Furutani, Y. Izumi, Y. Tanaka, K. Osaka, T. Morita and Y. Yoshimi, Photoinduced

Electron Transfer-Promoted Reactions Using Exciplex-Type Organic Photoredox Catalyst Directly Linking Donor and Acceptor Arenes, *Molecules*, 2019, **24**, 4453.

5 K. Y. Cohen, R. Evans, S. Dulovic and A. B. Bocarsly, Using Light and Electrons to Bend Carbon Dioxide: Developing and Understanding Catalysts for CO_2 Conversion to Fuels and Feedstocks, *Acc. Chem. Res.*, 2022, **55**, 944–954.

6 Y. He, L. Yin, N. Yuan and G. Zhang, Adsorption and activation, active site and reaction pathway of photocatalytic CO2 reduction: A review, *Chem. Eng. J.*, 2024, **481**, 148754.

7 D. M. Guldi, D. Langford, Y. Reva, A. Günay-Gürer, Y. Bo, K. Gubanov, L. Mai, R. W. Crisp, I. Engelmann, R. Fink, A. Kahnt, B. Jana, M. Wu and E. Spiecker, Improving Photocatalytic Hydrogen Generation via Polycitric Acid-based Carbon Nanodots, *Angew. Chem., Int. Ed.*, 2025, e202418626.

8 X. Chen, Y. Wei, W. Sun, X. Meng, S. Hao and Y. Gao, Turning off hydrogen evolution via an organic dye photosensitizer in aqueous acetonitrile solution during photocatalytic CO_2 reduction to CO, *Mol. Catal.*, 2021, **500**, 111299.

9 J.-W. Wang, L. Jiang, H.-H. Huang, Z. Han and G. Ouyang, Rapid electron transfer via dynamic coordinative interaction boosts quantum efficiency for photocatalytic CO_2 reduction, *Nat. Commun.*, 2021, **12**, 4276.

10 W. Tu, Y. Yang, C. Chen, T. Zhou, T. Li, H. Wang, S. Wu, Y. Zhou, D. O'Hare, Z. Zou and R. Xu, Cu–O/N Single Sites Incorporated 2D Covalent Organic Framework Ultrathin Nanobelts for Highly Selective Visible-Light-Driven CO_2 Reduction to CO, *Small Struct.*, 2023, **4**, 2200233.

11 C. Hao, J. Wang, H. Shi, H. Zhang, J. Zhao, B. Cao and P. Yang, NonCovalent Aggregation-Driven D-Band Engineering in Nickel Cocatalysts for Efficient CO2 Photoreduction, *Angew. Chem., Int. Ed.*, 2025, **64**, e202508683.

12 C. Hao, Y. Sun, H. Shi, H. Zhang, J. Zhao, H. Yang and P. Yang, Asymmetric aggregation enables red-light CO2 reduction with tunable activity and selectivity by intermolecular electronic coupling, *Appl. Catal., B*, 2024, **356**, 124222.

13 J. M. López-Nicolás and F. García-Carmona, Aggregation State and pKa Values of (E)-Resveratrol As Determined by Fluorescence Spectroscopy and UV-Visible Absorption, *J. Agric. Food Chem.*, 2008, **56**, 7600–7605.

14 L. Mencaroni, T. Bianconi, M. Aurora Mancuso, M. Sheokand, F. Elisei, R. Misra and B. Carlotti, Unlocking the Potential of Push-Pull Pyridinic Photobases: Aggregation-Induced Excited-State Proton Transfer, *Chem.–Eur. J.*, 2025, **31**, e202403388.

15 J. R. Kanicky and D. O. Shah, Effect of Premicellar Aggregation on the pKa of Fatty Acid Soap Solutions, *Langmuir*, 2003, **19**, 2034–2038.

16 K. Lei, D. Wang, L. Ye, M. Kou, Y. Deng, Z. Ma, L. Wang and Y. Kong, A Metal-Free Donor–Acceptor Covalent Organic Framework Photocatalyst for Visible-Light-Driven Reduction of CO_2 with H_2O, *ChemSusChem*, 2020, **13**, 1725–1729.

17 Y.-Z. Cheng, X. Ding and B.-H. Han, Porous Organic Polymers for Photocatalytic Carbon Dioxide Reduction, *ChemPhotoChem*, 2021, **5**, 406–417.

18 X. Yu, K. Gong, S. Tian, G. Gao, J. Xie and X.-H. Jin, A hydrophilic fully conjugated covalent organic framework for photocatalytic CO_2 reduction to CO nearly 100% using pure water, *J. Mater. Chem. A*, 2023, **11**, 5627–5635.

19 Y. Fu, X. Zhu, L. Huang, X. Zhang, F. Zhang and W. Zhu, Azine-based covalent organic frameworks as metal-free visible light photocatalysts for CO_2 reduction with H_2O, *Appl. Catal., B*, 2018, **239**, 46–51.

20 J. Cui, C.-X. Li, J. Zhou, Y. Hua, Z.-Y. Zhou and Z.-M. Su, A covalent organic framework integrating photocatalytic center and electron reservoir for photocatalytic CO_2 reduction to HCOOH, *Sep. Purif. Technol.*, 2024, **346**, 127466.

21 M. Hida and T. Sanuki, Studies of the Aggregation of Dyes. The Scope of Application of the Maximum-slope Method, *Bull. Chem. Soc. Jpn.*, 2006, **43**, 2291–2296.

22 H. Gao, G. Liu, Y. Zhu, Z. Wen, X. Liu, G. Wang and F. Li, An efficient photocatalytic CO_2 reduction system improved by emodin as a redox mediator, *Green Chem. Eng.*, 2023, **4**, 433–438.

23 S. Solar, W. Solar and N. Getoff, Kinetic and Spectroscopic Behaviour of Proflavin Transients Studied by Pulse Radiolysis, *Z. Naturforsch. A*, 1982, **37**, 1077–1082.

24 D. H. Nam and C. B. Park, Visible light-driven NADH regeneration sensitized by proflavine for biocatalysis, *ChemBioChem*, 2012, **13**, 1278–1282.

25 L. O. Kostjukova, S. V. Leontieva and V. V. Kostjukov, The vibronic absorption spectra and electronic states of proflavine in aqueous solution, *Comput. Theor. Chem.*, 2021, **1197**, 113144.

26 S. De Silvestri and P. Laporta, Time-resolved and steady-state fluorescence studies of excited-state proton-transfer reactions of proflavine, *Chem. Phys. Lett.*, 1984, **103**, 275–280.

27 T. Ghosh, T. Slanina and B. König, Visible light photocatalytic reduction of aldehydes by Rh(iii)–H: a detailed mechanistic study, *Chem. Sci.*, 2015, **6**, 2027–2034.

28 K. Ananthanarayanan, C. Selvaraju and P. Natarajan, Novel excited state proton transfer reaction observed for proflavine encapsulated in the channels of modified MCM-41, *Microporous Mesoporous Mater.*, 2007, **99**, 319–327.

29 M. P. Pileni and M. Graetzel, Light-induced redox reactions of proflavine in aqueous and micellar solution, *J. Phys. Chem.*, 1980, **84**, 2402–2406.

30 K. Kalyanasundaram and M. Grätzel, Proflavine-sensitized photoproduction of H2 from water with electron-donors and a colloidal redox catalyst, *J. Chem. Soc., Chem. Commun.*, 1979, 1137–1138, DOI: 10.1039/C39790001137.

31 J. Ong, J. W. L. Loke, H. L. Koh and W. Y. Fan, Proflavine-catalysed trifluoromethylation of α,β-unsaturated carbonyls, *Mol. Catal.*, 2022, **530**, 112587.

32 M. Forster and R. E. Hester, Resonance Raman investigation of the photoreduction of methylviologen with Ru(bpy)2+3

and proflavine as sensitizers, *Chem. Phys. Lett.*, 1982, **85**, 287–292.
33 J. Zhou, Y. Jia, X. Wang, M. Jia, H. Pan, Z. Sun and J. Chen, Excited-State Dynamics of Proflavine after Intercalation into DNA Duplex, *Molecules*, 2022, **27**, 8157.
34 F. Strieth-Kalthoff, M. J. James, M. Teders, L. Pitzer and F. Glorius, Energy transfer catalysis mediated by visible light: principles, applications, directions, *Chem. Soc. Rev.*, 2018, **47**, 7190–7202.